PAPER

Doxorubicin delivery performance of superparamagnetic carbon multi-core shell nanoparticles: pH dependence, stability and kinetic insight†

Adriano Santos Silva, [ID] [a] Jose Luis Diaz de Tuesta, [ID] *[b] Thais Sayuri Berberich,[a,b] Simone Delezuk Inglez,[b] Ana Raquel Bertão,[c] Ihsan Çaha [ID] [c] Francis Leonard Deepak, [ID] [c] Manuel Bañobre-López [ID] [c] and Helder Teixeira Gomes[a]

In the past decade, magnetic nanoparticles (MNPs) have been among the most attractive nanomaterials used in different fields, such as environmental and biomedical applications. The possibility of designing nanoparticles with different functionalities allows for advancing the biomedical applications of these materials. Additionally, the magnetic characteristics of the nanoparticles enable the use of magnetic fields to drive the nanoparticles to the desired sites of delivery. In this context, the development of new MNPs in new approaches for drug delivery systems (DDSs) for cancer treatment has increased. However, the synthesis of nanoparticles with high colloidal stability triggered drug delivery, and good biocompatibility remains a challenge. Herein, multi-core shell MNPs functionalized with Pluronic ® F-127 were prepared and thoroughly characterized as drug carriers for doxorubicin delivery. The functionalized nanoparticles have an average size of 17.71 ± 4.2 nm, high water colloidal stability, and superparamagnetic behavior. In addition, the nanoparticles were able to load 936 μg of DOX per mg of functionalized nanomaterial. Drug release studies at different pH values evidenced a pH-triggered DOX release effect. An increase of 62% in cumulative drug release was observed at pH simulating tumor endosome/lysosome microenvironments (pH 4.5) compared to physiological conditions (pH 7.4). In addition, an innovative dynamic drug delivery study was performed as a function of pH. The results from this test confirmed the pH-induced doxorubicin release capability of carbon multi-core shell MNPs. The validity of traditional kinetic models to fit dynamic pH-dependent drug release was also studied for predictive purposes.

Introduction

As a result of being a disease with multi-level complexities and variability, growing mortality, and incidence, cancer has become a public health problem.[1] Clinical treatments used so far in medicine include radiation therapy, surgical resection and, mostly, chemotherapy.[2] Although chemotherapy treatments present progress in treating several types of neoplasms, this method is limited by inadequate cell uptake, multidrug re-sistance and, especially, due to serious side effects.[3] For this reason, the cancer research field is currently focused on exploring new approaches to treat the disease and eliminate drawbacks in the current widely applied approaches.[4–9] Among the strategies studied in this enormous field, stimuli-responsive drug delivery systems have presented satisfactory results, improving the possibility of successful treatment compared with conventional chemotherapy. These systems respond to external environmental stimuli, such as pH, enzyme, temperature and magnetic field changes, as a trigger to deliver the drug to specific sites.[10–16] As the scientific community continues to fabricate and engineer new DDSs, the necessity to develop new types of advanced materials to overcome old barriers takes shape.

In recent years, much effort has been dedicated to synthesizing magnetic nanocomposites in an attempt to exploit their applications.[17–22] MNPs offer a great promise for biomedical research and clinical therapy applications, given their small

[a]Centro de Investigação de Montanha (CIMO), Instituto Politécnico de Bragança, Campus Santa Apolónia, 5300-253 Bragança, Portugal
[b]Universidade Tecnológica Federal do Paraná, Campus Ponta Grossa, 84017-220 Ponta Grossa, Paraná, Brazil. E-mail: jl.diazdetuesta@ipb.pt
[c]Advanced (Magnetic) Theranostic Nanostructures Lab, International Iberian Nanotechnology Laboratory, Av. Mestre Jose Veiga s/n, 4715-330 Braga, Portugal
†Electronic supplementary information (ESI) available. See DOI: https://doi.org/10.1039/d1nr08550f

size, which offers unique properties. The most relevant MNP properties for medical treatments are biocompatibility, inject-ability, controlled shape and size, and a high level of accumulation in target tissues or specific areas.[23–25] For biomedical applications such as magnetic resonance imaging (MRI), hyperthermia and drug delivery, nanoparticles with superparamagnetic behavior are required. Their capacity of losing magnetism after removal of the magnetic field brings advantages for their application in these approaches.[26,27] Multiple techniques have been developed to prepare iron nanoparticles, including thermal decomposition, sonochemical decomposition, vapor-phase condensation and solution combustion (SCS).[28–30] The synthesis of magnetic materials by solution combustion has become a promising candidate for the preparation of nanoparticles since it is considered a time/energy saving procedure.[31]

SCS is an efficient method for the preparation of oxide materials, being recognized as a potential route for the synthesis of iron oxide composites. In brief, SCS is a self-sustained exothermic redox reaction between an oxidizer and fuel in a homogeneous aqueous solution. Usually, oxidants are metal precursors themselves, like metal nitrates, sulfates, and carbonates. The fuel is any organic material, such as citric acid, urea, or glycine.[31,32] Briefly, SCS consists of three main steps: (i) formation of the combustion mixture, (ii) formation of the gel and (iii) combustion of the gel. In addition to the cost, SCS only needs simple instrumentation that can be easily scaled up, and products with various functionalities and structures can be obtained. The final products obtained by SCS are materials with high purity, high surface area, and optimum aggregation.[33]

In this work, iron oxide nanoparticles were synthesized by the SCS method and used as magnetic cores, which are further coated with carbon in multi-core shell structures. Carbon coating represents an excellent strategy to overcome drawbacks such as non-biocompatibility and toxicity of magnetic materials, making its biomedical applications feasible. The most applied materials prepared by carbon coating are core–shell (CS) and yolk–shell (YS) nanoparticles, for which the main difference is the presence of a void between the core and the shell in the case of the YS nanoparticles. When the coating enwraps several cores of a given material or different materials, the nanoparticles may be named multi-core shell structures. In addition to coating, MNPs were functionalized with nitric acid and Pluronic® F-127 (PF127) to increase the colloidal stability and obtain negatively charged particles, enabling them to have great affinity toward cationic drugs such as doxorubicin (DOX). DOX is a highly potent chemotherapeutic drug that has been used successfully to produce regression in a broad spectrum of cancers. The carbon structure with its unique bonds and negatively charged surface enables different electrostatic interactions between the drug and the material in solutions with distinct pH values. This interaction is very important for drug delivery in cancer therapy since it is well-known that cancerous tissues have an acidic pH.

Materials and methods

Chemicals

The reagents used in this study were iron(III) nitrate nonahydrate (99%, Sigma Aldrich, Germany), citric acid monohydrate (98.8%, WWR Chemicals, Belgium), ethanol absolute (99.8%, Fischer Chemical, South Africa), tetraethyl orthosilicate (TEOS, 98%, Fluka Chemika, Germany), 1,3-benzenediol (99%, Alfa Aesar, USA), methanal (37–38% wt%, PanReac, Spain), ammonia solution 28–30% (Merck, Germany), sodium hydroxide (98.73%, Fisher Chemical, U.K.), potassium bromide (99%, Merck, Germany), sodium dihydrogen phosphate hydrate (99%, V.P., Portugal), disodium hydrogen phosphate dihydrate (99.5%, Pronalab, Portugal), nitric acid (37 wt% Fisher Chemical, U.K.), Pluronic ® F-127 (MW = 12 600, PF127, Sigma-Aldrich, Germany), and doxorubicin hydrochloride (DOX, 98%, Discovery Fine Chemicals, Wimborne, U.K.). All reagents were used as received, and distilled water was used throughout this work.

Synthesis of multi-core shell MNPs

The synthesis of the MNPs was performed in four main steps as presented in Fig. 1: (i) synthesis of the superparamagnetic core, (ii) carbon coating, (iii) removal of silica (etching), and (iv) functionalization of the surface.

For the first step, the synthesis of superparamagnetic magnetite (Fe_3O_4) was achieved by solution combustion synthesis (SCS), as illustrated in Fig. S1† and described elsewhere.[33] Briefly, 10 mL of 12 mM citric acid ($C_6H_8O_7$) solution was added dropwise for 10 min using a peristaltic pump to 10 mL of 21 mM iron(III) nitrate solution. The resultant solution was heated at 80 °C in a drying oven for 6.5 h. The flask was placed in an oil bath heated using a magnetic stirring plate and subjected to N_2 flow (100 N cm^3 min^{-1}) for 1 h at room temperature to ensure an inert atmosphere therein. After N_2 circulation, the solution was heated at 180 °C for 3 h. The yielding product obtained was washed with distilled water until neutral
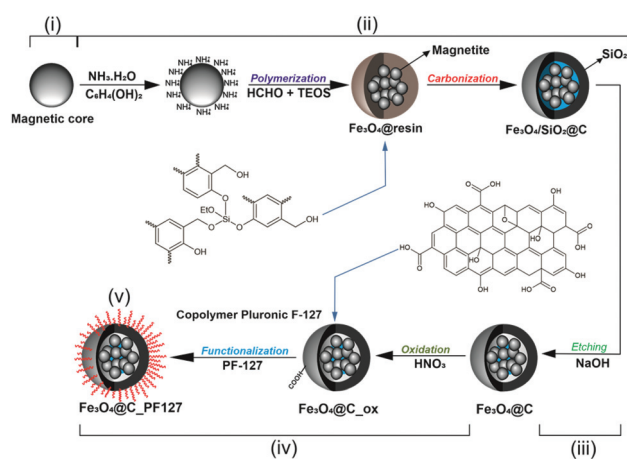

Fig. 1 Schematic representation of the synthesis steps of $Fe_3O_4@C\_PF127$.

pH by centrifugation at 6000 rpm for 5 minutes in an MPW-260R centrifuge (MPW Med. Instruments). The material was dried in an air oven overnight at 60 °C.

The carbon-based multi-core shell architecture was achieved in different stages: coating, carbonization, and etching. First, a one-pot strategy of hydrolysis and polymerization of TEOS and polymerization of the precursors resorcinol (1,3-benzenediol) and formaldehyde (methanal) was used by adapting the extended Stöber method described elsewhere.[34] Briefly, an ultrasonicated mixture of 0.25 g of magnetite with 50 mL of distilled water and 150 mL of absolute ethanol was added to a 500 mL three-necked bottom flask previously loaded with 0.10 g of resorcinol and 1.2 mL of ammonia solution (28–30%). The mixture was kept stirring for 1 h at 30 °C using a magnetic stirring plate with temperature control. Hereafter, 0.150 mL of formaldehyde solution (37–40%) and 0.210 mL of TEOS were added dropwise and the mixture was kept stirring for 6 h at the same temperature. After that, the temperature was increased to 80 °C and kept stirring at this temperature for 8 h. In the end, the solid sample was washed several times with distilled water by centrifugation at 6000 rpm for 5 min until the rinsing waters reached the neutrality of distilled water. The final washing was done with absolute ethanol, and the obtained solid was dried at 60 °C in a drying oven and named Fe_3O_4@resin.

At the end of the coating, the nanoparticles were covered with a shell made of the as-synthesized resin. For the carbonization step, the sample was annealed under an N_2 atmosphere in a vertical tubular furnace (ROS 50/250/12, Thermoconcept) at 120 and 400 °C for 1 h at each temperature, and then at 600 °C for 4 h, with a heating rate of 2 °C min^{-1} for the temperature ramps. The nanoparticles recovered from the furnace were named Fe_3O_4/SiO_2@C. In the final step, the resultant Fe_3O_4/SiO_2@C nanoparticles were etched under stirring with 10 M NaOH solution at room temperature for 16 h to remove the content of silica from the material. The product was washed several times by centrifugation with distilled water until the rinsing waters reached the neutrality of distilled water. The final washing was done with absolute ethanol, and the obtained solid was dried at 60 °C overnight in an air oven. The resultant carbon-coated material was denoted as Fe_3O_4@C.

The Fe_3O_4@C surface was functionalized to increase its colloidal stability and affinity with cationic drugs. For this purpose, the oxidation of the carbon-based shell was performed by mild acid treatment followed by the incorporation of PF127.[10] Briefly, MNPs were suspended in a nitric acid solution (1 M) with a concentration of 5 mg mL^{-1}, maintained under stirring for 3 h at 60 °C. After this treatment, the product was washed with distilled water several times by centrifugation at 6000 rpm for 5 minutes until the rinsing waters reached the neutrality of distilled water. The final washing was done with absolute ethanol, and the obtained solid was dried at 60 °C overnight in an air oven. Once the surface was activated with HNO$_3$, the resultant material named Fe_3O_4@C_ox (2 mg mL^{-1}) was functionalized with PF127 (40 mg mL^{-1}) for

5 h at room temperature under magnetic stirring. In the end, the functionalized nanoparticles were recovered by centrifugation at 13 000 rpm for 20 minutes and washed several times with distilled water to remove the unbound copolymer. The final nanomaterial (Fe_3O_4@C_PF127) was stored at 4 °C in distilled water with a concentration of 10 mg mL^{-1} until posterior utilization for drug loading and release tests.

Nanoparticle characterization

X-ray diffraction, Fourier Transform Infra-Red (FT-IR) spectroscopy, and textural properties were investigated to characterize the materials, following the methodologies described in previous work.[35] Briefly, the superparamagnetic core was characterized by XRD to perform phase identification and to determine the crystalline structure. In addition, the particle size was estimated using XRD data following the Halder–Wagner mathematical methodology, as described elsewhere.[36] Fe_3O_4@resin nanoparticles were also analyzed by XRD to identify possible interferences in the crystalline structure of the magnetite. XRD analysis was performed in a PANalytical X'Pert MPD equipped with an X'Celerator detector and a secondary monochromator (Cu Kα λ = 0.154 nm; data recorded at a 0.017° step size). The composition of the superparamagnetic core based on magnetite was identified using the HighScore software and the Crystallography Open Database. FT-IR analysis was performed using a Perkin Elmer Spectrum Two FT-IR spectrometer with Universal ATR at a resolution of 1 cm^{-1} and a scan range of 4000 to 450 cm^{-1}. For the analysis, pellets of the sample dispersed in KBr were prepared with 1 mg of nanomaterial and 100 mg of KBr. This mixture was pressed into a mold to form a pellet, with 8 tons of pressure for 3 minutes.

The samples were subjected to thermogravimetric analysis (TGA) (STA 449 Jupiter, Netzsch, Goa, India) to study the mass loss according to the temperature range and calculate the DTG results to corroborate with the discussion. Fe_3O_4, Fe_3O_4@resin, Fe_3O_4/SiO_2@C, and Fe_3O_4@C were analyzed under an air atmosphere from 50 to 950 °C, with a heating rate of 10 °C min^{-1}.

The textural properties of the MNPs were determined by analysis of N_2 adsorption–desorption isotherms at 77 K (Quantachrome NOVA TOUCH LX^4, equipped with long cells with a bulb and outer diameter of 9 mm). BET specific surface area (S_{BET}), total pore volume (V_T), and average diameter of micropore (D_{mic}) were determined with the aid of the Quantachrome TouchWin™ software, following the methods described elsewhere.[37] Transmission Electron Microscopy (TEM), Scanning Transmission Electron Microscopy (STEM) and energy-dispersive X-ray spectroscopy (EDX) were carried out with a double corrected FEI Titan G3 Cubed Themis equipped with a Super-X EDX System, operating at 200 kV. EDS mapping of C, O, Fe and Si was performed, with the following spectral lines: C Kα = 280 eV, O Kα = 524 eV, Fe Kα = 6403 eV, and Si Kα = 1741 eV.

To evaluate the stability of the nanoparticles, suspensions of functionalized nanomaterials in water, phosphate buffer solutions (PBS) of pH 4.5, 6.0, and 7.4, and 2 biological fluids

were monitored for 6 h. Biological fluids used were Dulbecco's Modified Eagle's Medium (DMEM) and DMEM with 1% of Fetal Bovine Serum (DMEM1). The concentration of the nanoparticles in the suspension was 1 mg mL^{-1}, and the stability of the MNPs in the fluids was followed by the acquisition of digital images at times of 0, 1, 2, 4 and 6 h. To confirm the stability and determine the average hydrodynamic diameter of the nanoparticles and surface charge, dynamic light scattering (DLS, Horiba SZ-100Z) and zeta potential measurement were carried out.

Relaxation times at a magnetic field of 1.41 T were measured using a Bruker minispec (mq 60) bench-top relaxometer operated at 60 MHz and 37 °C. Five water solutions (200 µL) of the carbon-coated magnetite nanostructures in the Fe concentration range 0.1–0.4 mM were measured using (i) a standard inversion recovery sequence for longitudinal relaxation time (T_1) determination, and (ii) a standard Carr–Purcell–Meiboom–Gill (CPMG) sequence for transverse relaxation time (T_2) calculation. The relaxivity constants (r_1 and r_2) were calculated from the slope of the curve obtained by fitting the $T_1{}^{-1}$ or $T_2{}^{-1}$ values *versus* the total Fe concentration in mM.

For r_2 calculation at 3 T a T_2 parametric map was acquired with a multi-echo-multisliced (MEMS) sequence with 10 echoes times (TE = 15, 30, 45, 60, 75, 90, 105, 120, 135 and 150 ms), a repetition time (TR) of 1400 ms and a number of averages (NA) = 10 using an MR Solutions Benchtop system (Guildford, UK) at 37 °C with matrix 256 × 252, a field of view (FOV) of 60 × 60 mm and 1 slice of 1 mm thickness. Post-processing was performed using the ImageJ software (Rasband, W. NIH) for the construction of T_2 maps, and r_2 was calculated from the slope of the curve obtained by fitting the $T_2{}^{-1}$ values *versus* the total Fe concentration in mM.

Drug loading and release

To assess the efficiency of the developed Fe$_3$O$_4$@C_PF127 as pH-dependent drug nanocarriers, a drug-delivery system was used to simulate the environment in which the drug is used. For this purpose, phosphate buffer solutions (PBS) were employed at different pH values, namely 4.5, 6.0, and 7.4. PBS at pH 4.5 was prepared using a solution of 0.05 M NaH$_2$PO$_4$·H$_2$O. The solutions of pH 6.0 and 7.4 were prepared according to the Promega Protocol & applications guide, using Na$_2$HPO$_4$·12H$_2$O and NaH$_2$PO$_4$·H$_2$O.[11]

Drug loading was carried out by mixing a DOX solution with a Fe$_3$O$_4$@C_PF127 suspension. For this purpose, 4 mL of DOX 5 g L^{-1} solution and 2 mL of Fe$_3$O$_4$@C_PF127 suspension (10 mg mL^{-1}) were separately added into 20 mL of PBS with pH 7.4. Then, both solutions were placed in an ultrasonic bath (Ultrasonic Compact cleaner 1 L, Powersonic PS01000A, NOTUS, Vrable, Slovakia) for 1 h until homogeneity. Afterward, the solutions were mixed and placed in an IKA ® KS 130 Basic orbital shaker for 48 h at room temperature with stirring (300 rpm). The resulting suspension was centrifuged at 6000 rpm for 5 minutes, and the bottom body containing Fe$_3$O$_4$@C_PF127 loaded with DOX (Fe$_3$O$_4$@C_PF127-DOX) was lyophilized and stored in a freezer until its use for drug release tests. To calculate the DOX concentration loaded on Fe$_3$O$_4$@C_PF127, the supernatant's absorption was measured at 480 nm in a UV-VIS spectrometer (T70 UV/VIS Spectrometer, PG Instruments Ltd, United Kingdom).

Drug release tests were carried out in duplicate for different PBS values at physiological (pH 7.4) and acidic pH levels (pH 4.5 and 6.0). To perform the release of the drug, around 2 mg of lyophilized freeze-dried Fe$_3$O$_4$@C_PF127 containing DOX were weighed and then added to 10 mL of PBS at different pH. The flasks were placed in an incubator (Shel Lab, USA) at 37 °C (average human body temperature) and stirred at 150 rpm for the tests. After 15 minutes, the mixture was centrifuged, and the concentration of the drug was measured by UV-VIS analysis at 480 nm. In the following, new PBS solutions were added to each one of the vessels to continue the study of drug release at different pH values. The process of centrifugation, analysis of the supernatant and reposition of PBS were repeated at times of 0.5, 1, 2, 4, 6, 24, 48, and 72 h.

An innovative dynamic drug release test was performed to assess the nanoparticles' capacity to deliver the drug in a more realistic scenario in which the nanocontainer would follow a path experiencing pH changes over time. For this test, 2 paths (path X and Y) with different pH values along 3 time zones ($y1$, $y2$, and $y3$) were explored to evaluate if Fe$_3$O$_4$@C_PF127 containing DOX could present the expected response, following the strategy presented in Fig. S2.† Accordingly, $y1$ was defined as the first 2 h of drug release, $y2$ was defined as the drug release between 2 and 6 h, and $y3$ represents the drug release between 6 and 72 h. For path X, pH 7.4 was used in the first time zone, changed to pH 6.0 in the second zone and completed with pH 4.5. For path Y, pH 6.0 was used in the first time zone, pH 7.4 in the second time zone, and pH 4.5 in the last one.

Magnetic resonance imaging

MR imaging was performed in a 3 T horizontal bore MR Solutions Benchtop system (Guildford, UK) equipped with 48 G cm^{-1} actively-shielded gradients. For imaging of the sample, a 56 mm diameter quadrature birdcage coil was used in transmit/receive mode. For the phantom measurements, 100 µL of Milli-Q-water nanoparticle solutions in the concentration range 0–50 µM (Fe) were imaged with an image matrix 256 × 252, a field of view (FOV) of 60 × 60 mm, and 2 slices with a slice thickness of 1 mm and a slice gap of 1 mm. For T_2-weighted imaging acquisition a fast spin echo (FSE) sequence with TE = 68 ms, TR = 4800 ms and NA = 10 was used. For T_1-weighted imaging a FSE sequence with TE = 11 ms, TR = 720 ms, and NA = 10 was used.

Calculation methods

The concentration of DOX loaded was calculated by the difference between the theoretical input DOX loading and the concentration of DOX in the supernatant. The DOX loading in Fe$_3$O$_4$@C_PF127 was expressed in terms of DLC (drug loading

capacity) and DLE (drug loading efficiency), calculated using eqn (1) and (2).

$$\text{DLC} = \frac{C_{\text{Fe}_3\text{O}_4@\text{C}_{\text{PF127}}\text{-DOX}}}{C_{\text{Fe}_3\text{O}_4@\text{C\_PF127}}} \quad (1)$$

$$\text{DLE}(\%) = \frac{C_{0,\text{DOX}} - C_{\text{f,DOX}}}{C_{0,\text{DOX}}} \times 100 \quad (2)$$

where $C_{\text{Fe}_3\text{O}_4@\text{C\_PF127-DOX}}$ is the concentration of DOX loaded in $\text{Fe}_3\text{O}_4@\text{C\_PF127}$ ($\mu\text{g mL}^{-1}$), $C_{\text{Fe}_3\text{O}_4@\text{C\_PF127}}$ is the concentration of $\text{Fe}_3\text{O}_4@\text{C\_PF127}$ (mg mL^{-1}), $C_{0,\text{DOX}}$ is the initial concentration of the drug solution before loading ($\mu\text{g mL}^{-1}$), and $C_{\text{f,DOX}}$ is the final concentration of the drug measured in the supernatant after loading ($\mu\text{g mL}^{-1}$). To determine the percentage of cumulative drug release (CDR) at each time, a calculation using the amount of DOX present in $\text{Fe}_3\text{O}_4@\text{C\_PF127}$-DOX through DLC was done. Considering M_T as the total mass of $\text{Fe}_3\text{O}_4@\text{C\_PF127}$-DOX used for experiments, M_0 as the initial mass of DOX loaded on $\text{Fe}_3\text{O}_4@\text{C\_PF127}$-DOX, CDR_t as the CDR for each time, and $M_{c,t}$ as the cumulative mass of DOX, the percentage can be calculated according to eqn (3) and (4).

$$M_0 = \frac{M_T \cdot \text{DLC}}{\text{DLC} + 1} \quad (3)$$

$$\text{CDR}_t = \frac{M_{c,t}}{M_0} \times 100 \quad (4)$$

Kinetic modelling was performed following the methods described in previous works.[38,39] Briefly, the equations were fitted using non-linear regression employing a successive numerical iteration based on a generalized reduced gradient algorithm for the least error sum of squared minimization of the dependent variable of each kinetic model. The models were evaluated by the determination factor (r^2) and the adjusted determination factor ($r^2_{\text{adjust.}}$) to take into account the degrees of freedom or the number of parameters from each model equation.[40] Prediction of CDR for pH-dependent path drug release was made using the kinetic models that best fit the experimental points.

Iron leaching from the magnetic core in drug release tests

Iron leaching from the superparamagnetic core and the $\text{Fe}_3\text{O}_4@\text{C\_PF127}$ sample was evaluated. In brief, 2 mg of nanoparticles were placed in 10 mL of PBS solutions with pH 7.4, 6.0, and 4.5 (the same PBS as those used for the drug release studies). This mixture remained in an incubator for 72 h at 37 °C, simulating the experiment performed for the drug release tests. In the end, the nanoparticles were recovered, and the liquid samples were used to measure iron concentration using atomic absorption spectroscopy (Varian SpectrAA 220).

Results and discussion

Textural properties and morphology of the synthesized MNPs

Adsorption isotherms of N_2 at 77 K for bare magnetite, $\text{Fe}_3\text{O}_4/\text{SiO}_2@\text{C}$, and $\text{Fe}_3\text{O}_4@\text{C}$ are shown in Fig. S3.† Isotherms can be classified as type IV, following the IUPAC classification of N_2 adsorption isotherms. This classification is attributed to the isotherms with a hysteresis loop, typically found for mesoporous materials. The hysteresis loop is classified as type H4, associated with narrow slit-like pores. The results obtained for textural properties for the materials are presented in each adsorption isotherm. The BET surface area increased about 123% after carbonization (from 35 to 78 $\text{m}^2 \text{ g}^{-1}$) when silica and the carbon shell were present in the material structure ($\text{Fe}_3\text{O}_4/\text{SiO}_2@\text{C}$). Surprisingly, the BET surface area further increased up to 239% (78 to 265 $\text{m}^2 \text{ g}^{-1}$) after removing silica by etching with 10 M NaOH (sample $\text{Fe}_3\text{O}_4@\text{C}$). The high increase is ascribed to the partial removal of silica from the interstitial space of the multi-core agglomeration.

Following the Stöber method, the hydrolysis and polymerisation of TEOS are favoured at the early stages of the reaction and, as the reaction processes are near completion, the polymerisation of resorcinol and formaldehyde became predominant, resulting in the formation of a phenolic resin polymer layer that is carbonized, etched and functionalized.[41] The chemical structure proposed for the resin and carbon shell presented in Fig. 1 was presented in other works reported in the literature.[10,41] With the purpose of observing the resultant material, TEM analysis was performed. The results obtained are given in Fig. S4a† for the magnetite synthesized by SCS and in Fig. S4b† for the functionalized sample ($\text{Fe}_3\text{O}_4@\text{C\_PF127}$). The particle size was calculated using the ImageJ software, and it was found to be 15.9 ± 2.7 nm for the bare magnetite agglomerates and 17.7 ± 4.2 nm for $\text{Fe}_3\text{O}_4@\text{C\_PF127}$. With these results, it is possible to estimate that the shell presents about 1.7 ± 6.9 nm of thickness. Further investigations were necessary to understand the final composition of the nanoparticle, and to evaluate the effect of the etching.

Representative STEM and TEM images confirm the core–shell structure of the developed nanoparticles before Si etching (Fig. 3(a) and Fig. S5†). Highly ordered crystalline domains are clearly observed in the magnetic core, which is compatible with a multi-core formed by smaller magnetite nanoparticles. The particle size was found below the single-to-multi-domain size transition, in agreement with the observed superparamagnetic properties of the sample. Fig. 3B shows a HAADF-STEM image of the same core–shell magnetic aggregate and an Energy-Dispersive X-ray (EDX) elemental analysis map highlighting the spatial distribution of the C, Fe, O and Si elements. The results confirm the amorphous carbon composition of the shell, as well as the iron oxide core, as deduced by the Fe and O spatial distribution which is restricted to the core volume. Likewise, Si is randomly distributed all over the inorganic magnetic core, pointing to an interstitial occupation. This is further confirmed by an EDX line scan analysis across the multi-core shell structure in Fig. 3C: whereas a higher density of C is observed within the shell thickness compared to the core. Fe, O and Si elemental density is localized only in the core, being null in the outer carbon shell. These results, together with the structural and magnetic results, confirm the

multi-core shell structure of nanoparticles with the chemical composition Fe$_3$O$_4$/SiO$_2$@C.

Representative HAADF-STEM and TEM images in Fig. S5(a–b) and S4† still show core–shell carbon-coated multi-core structures, where EDX elemental mapping analysis highlighted a C shell and a Fe/O rich multi-core (Fig. S5(c)†). Surprisingly, the etching process could not remove all the Si from the structure, which still can be observed in the inorganic cores. EDX line scan analysis along a core–shell structure confirms the presence of a C shell around several inorganic nuclei, where Fe, O and Si are uniformly distributed, Si being present in a significant much lower amount (Fig. S6(c)†). It is important to highlight that the etching process induces the partial crystallization of the carbon shell (mostly in the outer part), which resembles the crystalline structure of carbon nanotubes (see the TEM images of several representative core–shell nanostructures in Fig. S7†).

The difference in the total pore volume is even more significant, with an increase of about 276% through carbonization (143 mm^3 g^{-1} for Fe$_3$O$_4$/SiO$_2$@C and 38 mm^3 g^{-1} for Fe$_3$O$_4$) and 260% through the etching process (from 143 mm^3 g^{-1} for Fe$_3$O$_4$/SiO$_2$@C to 515 mm^3 g^{-1} for Fe$_3$O$_4$@C). Therefore, both the BET surface area and total pore volume increase after silica indicates the success of the synthesis protocol. The average pore diameter calculated was about the same for Fe$_3$O$_4$ and Fe$_3$O$_4$/SiO$_2$@C materials, with a significant increase for the Fe$_3$O$_4$@C nanomaterial.[41]

Thermal properties of the MNPs

TGA under an oxidative atmosphere and differential thermogravimetry were used to study the influence of the material structure on the mass loss at different temperatures and consequently to determine the effect of the different steps performed during the synthesis. The results obtained are presented in Fig. 2a. The curve for the core shows about 5% of mass loss, which agrees with the values reported in the literature, following the same method of synthesis known for the high purity materials obtained.[11] The peak in the DTG of the bare magnetite appearing at 400 °C can be ascribed to the removal of the low content of organic impurities from the material.

Fe$_3$O$_4$@resin is the coated core, for which the resultant material has a shell made of polymeric resin based on TEOS, resorcinol, and formaldehyde. Fe$_3$O$_4$@resin is the material with the highest mass loss (47% loss mass at 950 °C) among all studied samples (4%–20%), and this can be attributed majorly to the synthesized organic resin shell.[42] According to the polymerization process, a phenolic hybrid ceramic has been prepared with a three-dimensional cross-linked inorganic network structure based on covalent O-bonds between the organic (aromatic rings) and inorganic (Si) phases, as presented in Fig. 1. Accordingly, the sample may be thermally decomposed and oxidized during TGA assays. DTG results in Fig. 2b show different peaks observed during the resin degradation for this sample. The peak in the range of 80–120 °C represents the loss of adsorbed water, and the peak ranging from
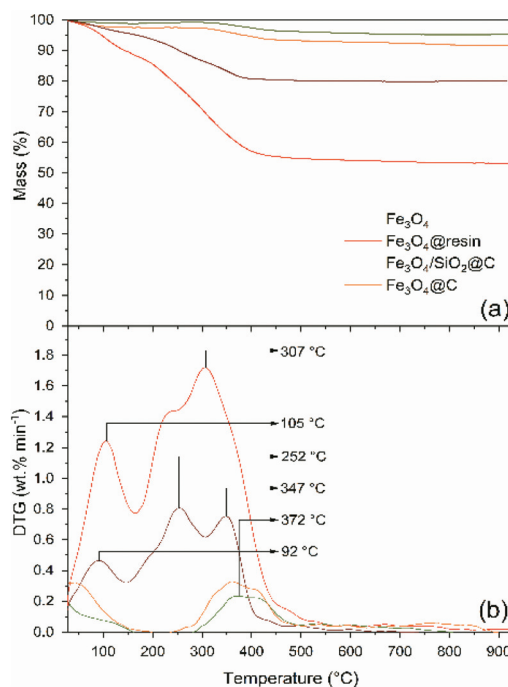
Fig. 2 Results of (a) TGA and (b) DTG for MNPs obtained at different synthesis stages.

200 to 400 °C represents both the decomposition of OH groups of silanols and the elimination of the organic content, coming from the phenolic hybrid ceramic.

After annealing in the N$_2$ atmosphere, SiO$_2$ occupies the interstitial space of the multi-core agglomeration, and the Fe$_3$O$_4$/SiO$_2$ nanoparticles are coated with a shell made of carbon, as shown in Fig. 1 and confirmed in Fig. 3. The formation of SiO$_2$ is of great importance to avoid the carbon coating reaching the multi-core and blocking useful surface area. SiO$_2$ is then used as a hard template to protect the multi-core from pore blocking, once its removal significantly increases the surface area as shown by the S_{BET} results after etching. Both TGA and DTG results show that after heat treatment under an inert atmosphere (Fe$_3$O$_4$/SiO$_2$@C), the nanomaterial achieved high stability since the mass loss was lower (20 wt%), which can be ascribed to the high degree of carbonization of the material. Again, the peak related to the loss of adsorbed water can be identified in DTG. The other peak represents the decomposition of OH groups of silanols, still present in the material structure.

Finally, the results obtained for the nanoparticle after etching (Fe$_3$O$_4$@C) present a lower mass loss than the previous one (9 wt%). The decrease in the mass loss can be ascribed to the removal of the silica, confirmed by the disappearance of the peak in the range 200–400 °C attributed to the elimination of OH groups of silanols. Beyond the detailed analysis of the modifications to the material at each step, it is also possible to calculate the percentage of carbon in the final material, which is around 5%.
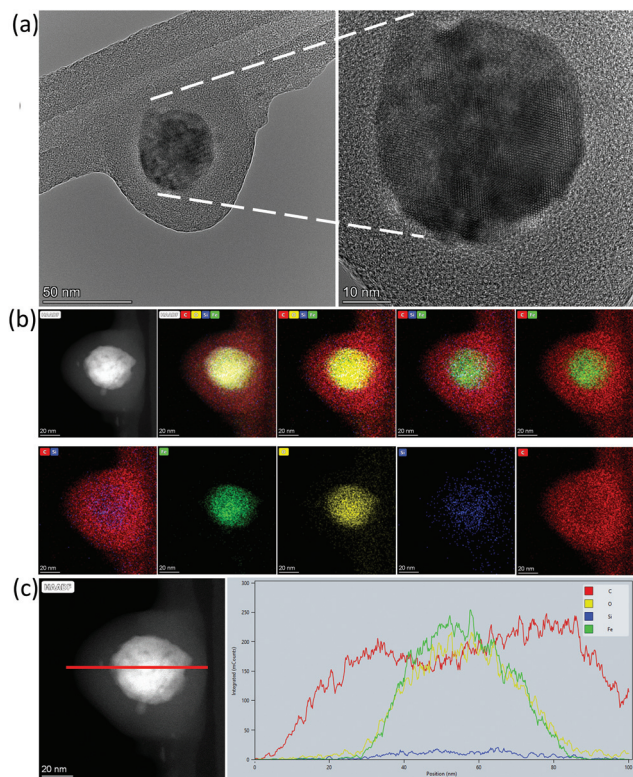
Fig. 3 Before Si etching (Fe₃O₄/SiO₂@C). (a) TEM image of a core–shell magnetic aggregate. The left inset shows a zoom-in showing the multi-domain crystalline structure of the magnetic core. (b) HAADF-STEM image of the same core–shell nanostructure and Energy-Dispersive X-ray (EDX) elemental mapping analysis showing the spatial distribution of C, Fe, O and Si elements in the structure. (c) STEM-EDX line scan analysis along a single core–shell nanostructure by measuring the intensity of the characteristic spectral lines of C, Fe, O and Si elements.

Crystallinity and magnetism of the core

XRD was used to characterize the crystallography of the superparamagnetic core of the synthesized magnetite before and after coating with the resin. The XRD spectrum presented in Fig. 6 shows characteristic peaks corresponding to the presence of magnetite,[43,44] as desired. The spectra for the coated nanoparticles (Fe₃O₄@resin) showed no significant changes in the inorganic structure since the peaks related to magnetite are still present after the procedure. From the XRD spectra of the pure superparamagnetic core, it is possible to calculate the particle size using the Halder–Wagner methodology described elsewhere,[36] and a particle size of 14.8 nm was obtained.

The magnetic hysteresis loop obtained for Fe₃O₄@C_PF127 is presented in Fig. 4a. The saturation magnetization for the functionalized nanoparticle reached a value of 46.5 emu g⁻¹. The thermal treatment performed during the synthesis steps can increase the magnetic characteristic of the nanomaterials. The results also show a strong superparamagnetic behaviour of the sample, as revealed by the magnified region of the graph (inset Fig. 4b) with low coercivity (H_c) and saturation remanence (M_r) values of 45 Oe and 2.89 emu g⁻¹, which can
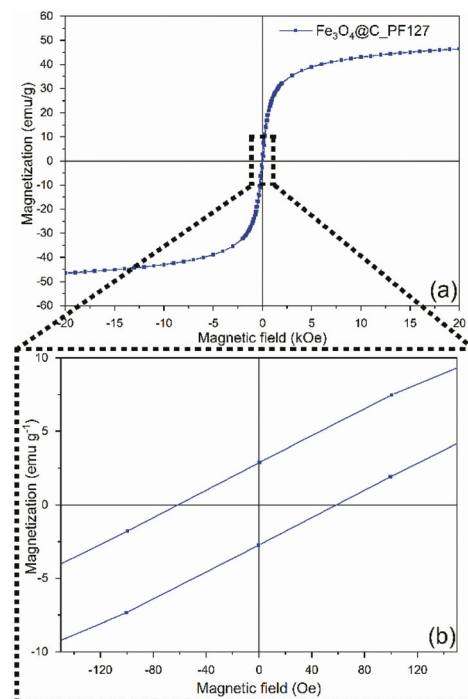

Fig. 4 Hysteresis loop for the core and Fe₃O₄@C_PF127, and (b) magnified region.

be attributed to the lower dipolar interaction between the cores due to the presence of a carbon-based shell.

Functionalization of the MNPs

FT-IR was carried out to recognize the chemical bonds in the structure, relate them with the treatments used during the synthesis, and study the effects of the functionalization at the material surface. A comparison of the spectra before and after functionalization is shown in Fig. 5. The presence of magnetite is noticed in the absorption bands at 564 cm⁻¹. The bands observed at 1632 and 3436 cm⁻¹ correspond to the bending and stretching vibrations of the surface –OH groups present in the carbon-based shell. The absorption bands at 1384, 1458,
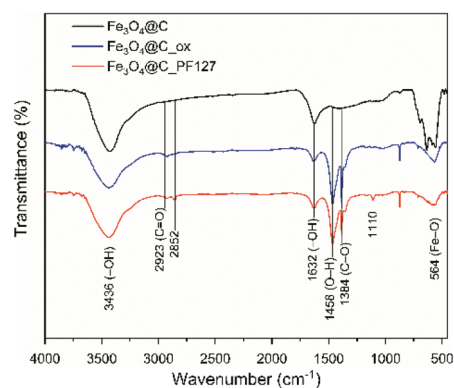
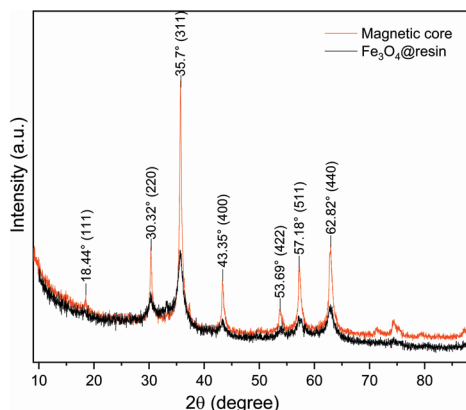Fig. 5 FTIR results for the functionalized and non-functionalized MNPs.

Fig. 6 XRD spectra of bare synthesized and coated magnetite.

and 2923 cm^{-1} may be ascribed to carboxylic acid groups in the samples, as expected after the oxidation with nitric acid. The bands at 1110 and 2852 cm^{-1} identified in the Fe$_3$O$_4$@C_PF127 nanomaterial are ascribed to the vibration of the Pluronic ® F-127 alkyl chain, confirming the presence of the copolymer in the final material. It is important to highlight that the presence of carboxylic groups remaining after functionalization with PF127 in the resultant nanomaterial (Fe$_3$O$_4$@C_PF127). Those functional groups are directly related to the enhancement of the colloidal stability of the final nanoparticles in aqueous solutions, a desirable characteristic for the biomedical applications of nanomaterials.

In particular, high colloidal stability is also a requirement for an injectable drug delivery system. With a very simple test, it was possible to analyze the colloidal behavior of Fe$_3$O$_4$@C_PF127 suspended in different media for 6 h. The images obtained in this test are shown in Fig. S8.† The results revealed the high stability of the suspension since no significant change was observed during more than 6 h of the test. Its high stability in aqueous media was confirmed by DLS analysis, as shown in Fig. 7. Through this analysis, the average hydrodynamic diameter (D_H) was determined to be 290 ± 41 nm, with a polydispersity index (PDI) of 0.344.[10] The zeta potential of functionalized nanoparticles was found to be −42.5 mV, which is in agreement with the good stability observed in the previous ana-
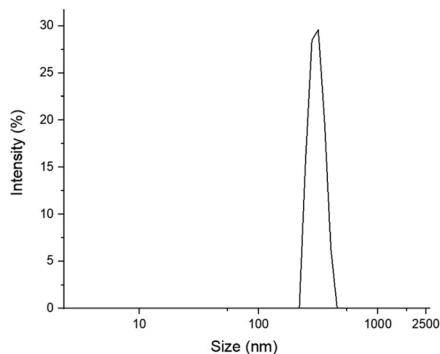
lysis. Furthermore, negatively charged nanoparticles are known to have increased circulation in blood by avoiding the oposination phenomenon and their elimination by macrophage cells.[45]

Drug release

The obtained values for DLC and DLE were 936 µg of DOX per mg of Fe$_3$O$_4$@C_PF127 and 93.6%, respectively, representing an improvement in the previous results involving MNPs synthesized *via* co-precipitation.[10] The pH values used were 4.5, 6.0, and 7.4 to investigate drug release conditions at an acidic level (simulating the acidic tumor environment and the acidic inside of intracellular vesicles, such as lysosomes where the nanoparticles could be cell internalized). The drug release results at the different pH values are shown in Fig. 8a.

The DOX release profile from Fe$_3$O$_4$@C_PF127 shows a strong dependence on pH. A higher cumulative release of the drug was observed as the pH decreased. The release profile followed the same tendency for distinct pH values, starting with a fast release in the first 4 h (first stage), followed by slow release until the end of the experiment (second stage). The results for drug delivery in the first stage revealed a very low amount of DOX released at pH 7.4 (8.3%), which simulates the physiological pH. At pH 6.0, DOX release was higher than in the simulated physiological environment pH, reaching 30% after 72 h of the experiment. Finally, the most acidic pH considered for the drug delivery tests (pH = 4.5) achieved the
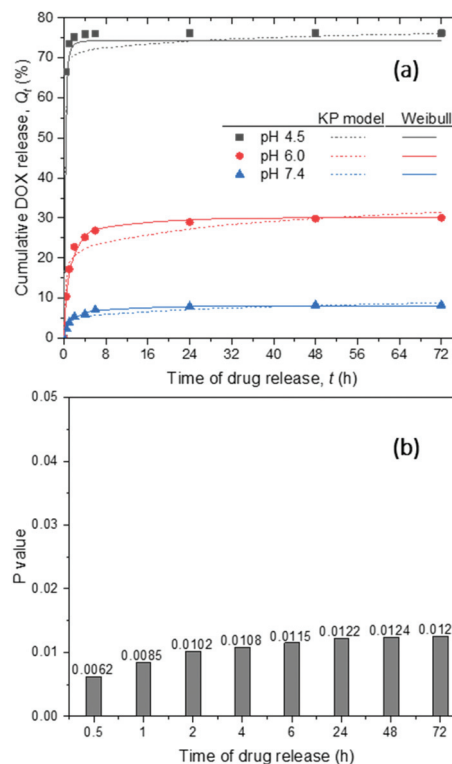

Fig. 7 Dynamic light scattering results of Fe$_3$O$_4$@C_PF127.

Fig. 8 (a) Drug release results using 0.2 mg mL^{-1} Fe$_3$O$_4$@C_PF127 at 37 °C in PBS solutions at different pH values (parameters for Weibull and Korsmeyer–Peppas kinetic models are summarized in Table 1); (b) *P*-value at each time for pH-dependent drug release tests.

highest amount of DOX delivery, reaching 76.2% after 72 h of drug release time.

The main reason for the triggered pH release observed with these specific nanoparticles is the π–π stacking interactions between the carbon-based nanocarriers and the aromatic DOX molecules, which are easily disrupted under a mildly acidic environment. In addition, the drug release in a mildly acidic environment is also favoured by the increased stability of DOX in the acid medium due to the protonation process.[46] The materials used in this work follow a procedure similar to the previous materials used for the same purpose, changing the method used to prepare the nanoparticle core. For instance, in earlier work,[11] the highest drug delivery achieved after 72 h was close to 20%, showing that Fe_3O_4@C_PF127 presents better performance than previously reported magnetite nanoparticles synthesized by different methods.

An ANOVA test was performed at different times to statistically evaluate if the amount of drug delivered into the system is significantly different at the proposed pH values. Fig. 8b illustrates the P-value obtained at each time. The results for the test can prove mathematically that the release is significant at all times, considering the amount of drug delivered at different pH values (95% confidence). Another interesting aspect of this result is that the P-value grows together with time, and this can be ascribed to the fact that drug delivery results present higher differences in the first stage of drug release. When the system goes through a steady-state (*i.e.*, reaching a plateau shape on the curve), the differences become smaller, reflecting the value obtained for the analysis for the statistical significance. Despite this difference being lower at the end of the experiment, it is possible to observe that the results remain different, reinforcing the pH-triggered drug release effect.

Semi-empirical drug release kinetic models such as zero and first order, Higuchi, Baker–Lonsdale, Korsmeyer–Peppas (KP), and Weibull models (represented by eqn (5), (6), (7), (8), (9), and (10), respectively) were used to fit the drug release pro-

files at different pH values and gain insights about the drug release kinetics.

$$Q_t = Q_0 + k_0 \times t \qquad (5)$$

$$\ln Q_t = \ln Q_{0.5} + k_1 \times t \qquad (6)$$

$$Q_t = k_H \times \sqrt{t} \qquad (7)$$

$$\left(\frac{3}{2}\right) \cdot \left(1 - \left(1 - \frac{Q_t}{Q_\infty}\right)^{2/3}\right) - \frac{Q_t}{Q_\infty} = k_{BL} \times t \qquad (8)$$

$$\frac{Q_t}{Q_\infty} = k_{KP} \times t^n \qquad (9)$$

$$\frac{Q_t}{Q_\infty} = 1 - \exp\left(-\frac{(t - T_i)^\beta}{\alpha}\right) \qquad (10)$$

where Q_t is the amount of drug released at time t; Q_0 is the initial amount of drug that is 0; $Q_{0.5}$ is the amount at 0.5 h (used for the first-order model); k_0 is the zero-order constant; k_1 is the first-order constant; Q_∞ is the amount of drug released at the equilibrium state (here considered as 72 h); k_H, k_{KP}, and k_{BL} are the release constants of Higuchi, Korsmeyer–Peppas, Baker–Lonsdale, respectively; and α, β and T_i denote the scale parameters of the Weibull model that describe the time dependence, shape of the dissolution curve progression and the latency time of the release process (here consider as T_i = 0 h), respectively. The results obtained for the fitness of kinetic models to experimental data are expressed in Table 1.

Zero-order, first-order, and Higuchi models have very low r^2 values, with some advantage for the Higuchi model followed by first-order. The results obtained for zero-order fitting suggest that the release of the active agent is not only dependent on time but also probably on the active agent concentration inside nanoparticles.[47] For first order and Higuchi models, the results demonstrate that the release profile is not completely dependent on concentration or is controlled by diffusion behavior. r^2 obtained for the Baker and Lonsdale

Table 1 Kinetic parameters obtained through the fitness of the kinetic models to the experimental data in the DOX release using 0.2 mg mL^{-1} of Fe_3O_4@C_PF127-DOX at 37 °C in PBS solutions at different pH values

Model	pH 4.5	pH 6.0	pH 7.4
Zero-order	$k_0 = 10.02$ h^{-1}	$k_0 = 3.92$ h^{-1}	$k_0 = 0.903$ h^{-1}
	$r^2 = r_{adjust.}^2 = 0.090$	$r^2 = r_{adjust.}^2 = 0.358$	$r^2 = r_{adjust.}^2 = 0.449$
First-order	$k_1 = 0.002$ h^{-1}	$k_1 = 0.019$ h^{-1}	$k_1 = 0.024$ h^{-1}
	$r^2 = r_{adjust.}^2 = 0.166$	$r^2 = r_{adjust.}^2 = 0.334$	$r^2 = r_{adjust.}^2 = 0.400$
Higuchi	$k_H/Q_\infty = 0.176$ h$^{-0.5}$	$k_H/Q_\infty = 0.164$ h$^{-0.5}$	$k_H/Q_\infty = 0.160$ h$^{-0.5}$
	$r^2 = r_{adjust.}^2 = 0.199$	$r^2 = r_{adjust.}^2 = 0.564$	$r^2 = r_{adjust.}^2 = 0.663$
Baker–Lonsdale	$k_{BL} = 9.56 \times 10^{-3}$ h^{-1}	$k_{BL} = 8.69 \times 10^{-3}$ h^{-1}	$k_{BL} = 8.19 \times 10^{-3}$ h^{-1}
	$r^2 = r_{adjust.}^2 = 0.090$	$r^2 = r_{adjust.}^2 = 0.358$	$r^2 = r_{adjust.}^2 = 0.449$
Korsmeyer–Peppas (KP)	$k_{KP} = 0.941$ h^{-n}	$k_{KP} = 0.635$ h^{-n}	$k_{KP} = 0.532$ h^{-n}
	$n = 0.0200$	$n = 0.117$	$n = 0.166$
	$r^2 = 0.992$	$r^2 = 0.905$	$r^2 = 0.921$
	$r_{adjust.}^2 = 0.991$	$r_{adjust.}^2 = 0.889$	$r_{adjust.}^2 = 0.908$
Weibull	$\alpha = 0.306$ h	$\alpha = 1.27$ h	$\alpha = 1.65$ h
	$\beta = 0.649$	$\beta = 0.666$	$\beta = 0.681$
	$r^2 = 0.999$	$r^2 = 0.992$	$r^2 = 0.994$
	$r_{adjust.}^2 = 0.999$	$r_{adjust.}^2 = 0.991$	$r_{adjust.}^2 = 0.993$

model was low because this model was developed based on Higuchi's model, and in this work, diffusion behavior is not the driving agent in drug release.[48] The Korsmeyer–Peppas model fitted better than previous ones because, in this empirical model, the assumption is that the release mechanism is rather not known or even dependent on more than one type of drug release phenomenon.[49]

Finally, the model with the best fit with experimental data was the Weibull model. For all pH values, the scale parameter β was below 1, which means the release profile is parabolic and displays a high initial slope and a consistent exponential character.[50] Parity plots were done for all the models following the strategy used in previous works to analyze how good models represent concentration trends, and the result is illustrated in Fig. S9.† [51,52] The Weibull and Korsmeyer–Peppas model results are presented together (Fig. S9a, S9b, and S9c†) to show that both models predict CDR significantly better than other models found in the literature (Fig. S9d, S9e, and S9f†).

Comparing the kinetic constants obtained in this work with the others from the literature is however complicated since most works present the values without unities.[53–56] Despite different results for model fitting, which is comprehensible considering most models were developed based on specific considerations about release characteristics, a tendency could be observed for all kinetic constants. In Fig. S10,† normalized kinetic constants (regarding maximum value for each pH) obtained for each model are represented. As observed in Fig. S10,† kinetic constants followed a tendency even for models with low r^2 values. k_0 (zero-order), k_H (Higuchi), k_{BL} (Baker–Lonsdale), and k_{KP} (Korsmeyer–Peppas) are parameters that decrease as pH increases; and k_1 (first-order), n (Korsmeyer–Peppas), α and β increase with increasing pH. To the best of our knowledge, no other work has addressed this analysis before.

Drug release during pH paths

Considering real application scenarios, the fluid carrying the drug loaded nanoparticles would be introduced into the patient. The nanoparticles would travel through the body directed by magnetic fields to successfully deliver the drug content to specific sites. In this regard, nanoparticles could experience different pH values along the pathway. The drug delivery experiment performed before was useful for evaluating the pH-triggered drug release capacity of the nanoparticles but is not enough to understand the real ability of the nanoparticles for real case applications. For this reason, another experiment was considered to analyze the nanoparticle behavior when exposed to different pH values during a 72 h drug delivery experiment. The results obtained with two different pH-dependent paths are shown in Fig. 9.

The results for drug release in this experiment reinforced the pH-dependent release nature achieved with the use of these nanoparticles and the capacity to deliver a higher amount of DOX in an acidic medium. The behavior followed the expected result for each time zone. In the first time zone, $y1$, a higher delivery of DOX in path Y can be observed com-
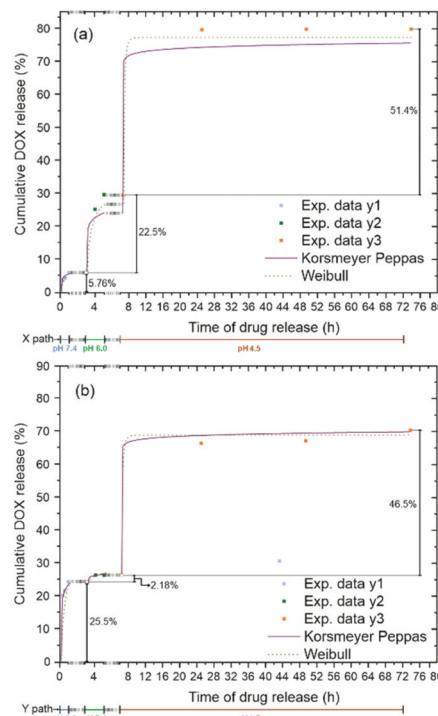

Fig. 9 pH-Dependent path drug release tests for (a) X path and (b) Y path (Weibull and Korsmeyer–Peppas kinetic models are presented).

pared to path X (5.76% for X vs. 25.51% for Y), ascribed to the more acidic environment in path Y in this time zone. In the second time zone, $y2$, the situation changes since path X has a more acidic environment, achieving a higher release of DOX than path Y in the same time zone (22.55% for X vs. 2.18% for Y). The same pH was used for the different paths in the last time zone, and the DOX delivery achieved the highest values for both tests. Surprisingly, CDR reached about 79% in path X and 75% in path Y, with a higher release for path X in this time zone (51.45% for path X vs. 46.55% for path Y). Higher release for path X with the same pH as path Y can be explained because the nanoparticles in path X had more drug loaded than path Y when the time zone $y3$ started in each experiment. This assay successfully confirms the pH-dependence on DOX release for DOX-loaded Fe_3O_4@C_PF127 nanoparticles. To the best of our knowledge, no other work has explored the ability of the nanomaterials to deliver the cargo experiencing pH changes throughout the experiment.

The prediction of drug release with a pH-dependent path was performed using kinetic models that best fit previous drug release results. Both models used for pH-dependent path drug release presented good fitting with experimental data, with r^2 values of 0.998 and 0.975 for Weibull and Korsmeyer–Peppas models in path X (Fig. 9a), and 0.999 and 0.997 for Weibull and Korsmeyer–Peppas models in path Y (Fig. 9b).

Magnetic resonance imaging

The inherent magnetic properties of certain nanostructured nanoparticles have been conventionally exploited for bio-

imaging applications. In particular, iron oxide nanoparticles of different sizes have been demonstrated to offer non-invasive MR imaging contrast enhancement, predominantly as a T_2 contrast agent, and also as a T_1 contrast agent in the case of ultra-small magnetite nanoparticles. In order to evaluate the MRI properties of the carbon-coated magnetite nanostructures, the longitudinal and transversal relaxivities (r_1 and r_2, respectively) were calculated at a low magnetic field of 1.41 T. The results showed an r_2 which was >40 fold higher than r_1 (r_2 = 180 mM^{-1} s^{-1}, r_1 = 4.3 mM^{-1} s^{-1}), indicating the preferential T_2 – behaviour of the nanostructures (Fig. S11A†). In fact, the r_2 value obtained was higher than that of Feridex (120 mM^{-1} s^{-1} at 1.5 T), a commercially used contrast agent based on iron oxide nanoparticles.

In order to translate these relaxivity values into real MR imaging in the clinical field of 3 T, both T_1 and T_2 weighted images were acquired in a phantom using an increasing concentration of nanoparticles (Fig. 10(a)). The results indicate a concentration-dependent contrast enhancement effect in the T_2-acquisition mode (>60% MRI signal reduction at 50 μMFe), whereas a null signal increase was observed in the T_1-acquisition mode in the whole range of Fe concentrations (Fig. 10(b)). This further confirms the T_2-MRI dark contrast effect and points to these carbon-coated magnetic nanostructures as suitable T_2-MRI (negative) contrast agents. In addition, a T_2 parametric map was acquired in which a progressive reduction of the T_2-relaxation time was observed as the Fe concentration increased in the samples (Fig. 10(a)). Also, r_2 (3 T) was calculated to be 227 mM^{-1} s^{-1} (Fig. S11B†), 26% higher than the value at 1.41 T, which can be explained by the increase of the magnetic field and the subsequent higher saturation magnetization of the magnetic nanoparticles at 3 T.

Iron leaching of the nanoparticles in drug release tests

Iron leaching from Fe_3O_4 and Fe_3O_4@C_PF127 samples were studied to evaluate the chemical stability of the nanocarrier in the drug release experiments. Considering the application of the nanomaterials, such evaluation is very important since the liberation of iron into the organism during a given treatment is not desirable. Iron leaching from bare magnetite showed to be inversely proportional to pH since the iron concentration

decreased with increasing pH reaching values of 1.93, 1.45, and 0.99 mg L^{-1} at pH 4.5, 6.0, and 7.4, respectively. Those iron concentrations in the liquid media are related to 2.76, 2.08, and 1.42 wt% mass loss of the magnetite at pH 4.5, 6.0, and 7.4, respectively. Surprisingly, iron leaching for functionalized nanoparticles (Fe_3O_4@C_PF127) resulted to be negligible at all pH values tested. These results demonstrate that carbon coating provides chemical stability to the magnetic carrier and protects MNP from degradation once iron was not detected in solution after 72 h at different pH values. Additionally, the utilization of Fe_3O_4@C_PF127 for real treatment approaches would not have problems associated with iron leaching.

Conclusions

Multi-core shell carbon-coated MNPs were prepared and successfully applied as drug carriers for DOX delivery. The use of SCS, a greener methodology, to synthesize a magnetic core allowed us to obtain superparamagnetic nanoparticles with a size of 15.94 ± 2.7 nm. In addition, functionalization with nitric acid and Pluronic ® F-127 increased the stability of the material in water, an important characteristic when considering its application for biomedical purposes. High colloidal stability was confirmed by stability tests with different media, DLS and zeta potential. Conventional drug release results demonstrated the capacity of the nanoparticles to release the drug in a more acidic environment, which reinforces the potential application of the nanoparticles for DDs applied to cancer treatment. The kinetic study performed in this work showed the dependence of the kinetic constant on pH for all models, and results with two best fits could be used to predict CDR in the second drug release test. Drug release profiles at different pH levels, static and dynamic changes, and ANOVA mathematical analysis confirmed the pH-triggered effect of the drug release process. Using a pH-dependent path drug delivery test where the pH varies along with the test, it was possible to confirm that Fe_3O_4@C_PF127 can preferentially release the drug in an acidic environment. The main purpose of this test was to expose the nanoparticles to a more realistic scenario, in which the nanoparticles would experience pH changes over time. Surprisingly, in the end, Fe_3O_4@C_PF127 delivered about the same amount of DOX, even after following different paths. Additionally to the innovative drug release test presented herein, iron leaching in drug release tests was also studied in this work. The result obtained demonstrates that Fe_3O_4@C_PF127 does not release iron into water, confirming the carbon coating as a shell protecting the magnetic cores from degradation and ensuring their safe use as DDSs.
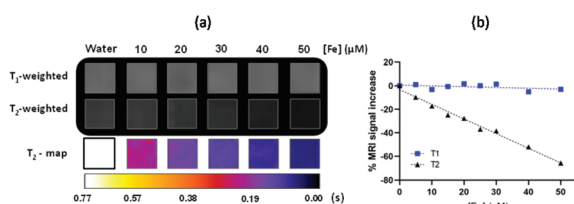
Fig. 10 (a) T_1 and T_2 weighted images and coloured T_2 parametric map of a phantom containing water solutions of carbon-coated nanoparticles at increasing nanoparticle concentrations acquired at 3 T. (b) MRI signal increase quantification (%) as a function of the Fe concentration according to the signal intensity observed in the T_1 and T_2 weighted images at 3 T.

Author contributions

Conceptualization: H. T. G. and J. L. D. T.; methodology: J. L. D. T. and A. S. S.; investigation: A. S. S., T. S. B., A. R. B. and I. Ç.; resources: H. T. G.; data curation: A. S. S. and

Conflicts of interest

There are no conflicts to declare.

Acknowledgements

References

1 C. Wild, E. Weiderpass and B. Stewart, *World Cancer Report: Cancer Research for Cancer Prevention*, Lyon, France, 2020th edn, 2020.

2 L. Liu, H. Jiang, J. Dong, W. Zhang, G. Dang, M. Yang, Y. Li, H. Chen, H. Ji and L. Dong, *Colloids Surf., B*, 2020, **185**, 110590.

3 L. Deng, Z. Liu and L. Li, *Hybrid nanocomposites for imaging-guided synergistic theranostics*, Elsevier Inc., 2019.

4 S. F. Medeiros, A. M. Santos, H. Fessi and A. Elaissari, *Int. J. Pharm.*, 2011, **403**, 139–161.

5 L. Bălăiță and M. Popa, *Rev. Roum. Chim.*, 2009, **54**, 185–199.

6 A. Andrade, R. Ferreira, J. Fabris and R. Domingues, Coating Nanomagnetic Particles for Biomedical Applications, in *Biomedical Engineering- Frontiers and Challenges*, 2011, DOI: **10.5772/19519**.

7 Q. Guo and C. Jiang, *Acta Pharm. Sin. B*, 2020, **10**, 979–986.

8 X. Fang, J. Cao and A. Shen, *J. Drug Delivery Sci. Technol.*, 2020, **57**, 101662.

9 Z. Gu, C. G. Da Silva, K. van der Maaden, F. Ossendorp and L. J. Cruz, *Pharmaceutics*, 2020, **12**, 1–25.

10 R. O. Rodrigues, G. Baldi, S. Doumett, L. Garcia-hevia, J. Gallo, M. Bañobre-lópez, G. Dra, R. C. Calhelha, I. C. F. R. Ferreira, R. Lima, H. T. Gomes and A. M. T. Silva, *Mater. Sci. Eng., C*, 2018, **93**, 206–217.

11 J. Oliveira, R. Rodrigues, L. Barros, I. Ferreira, L. Marchesi, M. Koneracka, A. Jurikova, V. Zavisova and H. Gomes, *C*, 2018, **5**, 1.

12 X. Gao, Z. Yu, B. Liu, J. Yang, X. Yang and Y. Yu, *Eur. Polym. J.*, 2020, **133**, 109779.

13 F. Bahrami, M. J. Abdekhodaie, F. Behroozi and M. Mehrvar, *J. Drug Delivery Sci. Technol.*, 2020, **57**, 101510.

14 R. Jahanban-Esfahlan, B. Massoumi, M. Abbasian, A. Farnudiyan-Habibi, H. Samadian, A. Rezaei, H. Derakhshankhah and M. Jaymand, *Polym. Technol. Mater.*, 2020, **59**, 1492–1504.

15 S. Motamedi, B. Massoumi, M. Jaymand and H. Hamishehkar, *J. Polym. Res.*, 2020, **27**(9), 272.

16 P. Xie and P. Liu, *Carbohydr. Polym.*, 2020, **236**, 116093.

17 Y. Liu, M. Li, F. Yang and N. Gu, *Sci. China Mater.*, 2017, **60**, 471–486.

18 S. Ayyanaar, M. P. Kesavan, C. Balachandran, S. Rasala, P. Rameshkumar, S. Aoki, J. Rajesh, T. J. Webster and G. Rajagopal, *Nanomedicine*, 2020, **24**, 102134.

19 A. Amani, J. M. Begdelo, H. Yaghoubi and S. Motallebinia, *J. Drug Delivery Sci. Technol.*, 2019, **49**, 534–546.

20 M. Ayubi, M. Karimi, S. Abdpour, K. Rostamizadeh, M. Parsa, M. Zamani and A. Saedi, *Mater. Sci. Eng., C*, 2019, **104**, 109810.

21 X. Xie, L. Zhang, W. Zhang, R. Tayebee, A. Hoseininasr, H. H. Vatanpour, Z. Behjati, S. Li, M. Nasrabadi and L. Liu, *J. Mol. Liq.*, 2020, **309**, 113024.

22 C. Boyer, M. R. Whittaker, V. Bulmus, J. Liu and T. P. Davis, *NPG Asia Mater.*, 2010, **2**, 23–30.

23 P. M. Price, W. E. Mahmoud, A. A. Al-Ghamdi and L. M. Bronstein, *Front. Chem.*, 2018, **6**, 1–7.

24 Y. H. Bae and K. Park, *Adv. Drug Delivery Rev.*, 2020, **158**, 4–16.

25 J. S. Basuki, H. T. T. Duong, A. Macmillan, R. B. Erlich, L. Esser, M. C. Akerfeldt, R. M. Whan, M. Kavallaris, C. Boyer and T. P. Davis, *ACS Nano*, 2013, **7**, 10175–10189.

26 I. Khan, K. Saeed and I. Khan, *Arabian J. Chem.*, 2019, **12**, 908–931.

27 Y.-H. Son, J.-K. Lee, Y. Soong, D. Martello and M. Chyu, *Chem. Mater.*, 2010, **22**, 2226–2232.

28 D. W. Lee, J. H. Yu, T. S. Jang and B. K. Kim, *Mater. Lett.*, 2005, **59**, 2124–2127.

29 V. Harnchana, A. Phuwongkrai, C. Thomas and V. Amornkitbamrung, *Mater. Today: Proc.*, 2018, **5**, 13995–14001.

30 R. Ianoş, A. Tăculescu, C. Păcurariu and I. Lazău, *J. Am. Ceram. Soc.*, 2012, **95**, 2236–2240.

31 M. Huang, M. Qin, Z. Cao, B. Jia, P. Chen, H. Wu and X. Wang, *Chem. Phys. Lett.*, 2016, **657**, 33–38.

32 F. T. Li, J. Ran, M. Jaroniec and S. Z. Qiao, *Nanoscale*, 2015, **7**, 17590–17610.

33 F. Deganello and A. K. Tyagi, *Prog. Cryst. Growth Charact. Mater.*, 2018, **64**, 23–61.

34 C. Jin, Y. Wang, H. Tang, H. Wei, X. Liu and J. Wang, *J. Phys. Chem. C*, 2014, **118**, 25110–25117.

35 A. S. Silva, M. S. Kalmakhanova, B. K. Massalimova, J. L. D. de Tuesta and H. T. Gomes, *Catalysts*, 2019, **9**, 705.

36 D. Nath, F. Singh and R. Das, *Mater. Chem. Phys.*, 2020, **239**, 122021.

37 J. L. Diaz De Tuesta, M. C. Saviotti, F. F. Roman, G. F. Pantuzza, H. J. F. Sartori, A. Shinibekova, M. S. Kalmakhanova, B. K. Massalimova, J. M. T. A. Pietrobelli, G. G. Lenzi and H. T. Gomes, *J. Environ. Chem. Eng.*, 2021, **9**, 105004.

38 J. L. Diaz de Tuesta, F. V. M. de Almeida, J. R. P. Oliveira, P. Praça, M. C. Guerreiro and H. T. Gomes, *Environ. Technol. Innov.*, 2021, **24**, 101984.

39 J. L. Diaz de Tuesta, A. Quintanilla, J. A. Casas, S. Morales-Torres, J. L. Faria, A. M. T. Silva and H. T. Gomes, *Catal. Today*, 2020, **356**, 216–225.

40 J. L. Diaz de Tuesta, A. M. T. Silva, J. L. Faria and H. T. Gomes, *Chem. Eng. J.*, 2018, **347**, 963–971.

41 W. J. Liu, Y. X. Liu, X. Y. Yan, G. P. Yong, Y. P. Xu and S. M. Liu, *J. Mater. Chem. A*, 2014, **2**, 9600–9606.

42 A. V. Korobeinyk, R. L. D. Whitby, J. J. Niu, Y. Gogotsi and S. V. Mikhalovsky, *Mater. Chem. Phys.*, 2011, **128**, 514–518.

43 E. C. Nnadozie and P. A. Ajibade, *Mater. Lett.*, 2020, **263**, 127145.

44 M. K. Shahid and Y. Choi, *J. Magn. Magn. Mater.*, 2020, **495**, 165823.

45 R. O. Rodrigues, G. Baldi, S. Doumett, L. Garcia-Hevia, J. Gallo, M. Bañobre-López, G. Dražić, R. C. Calhelha, I. C. F. R. Ferreira, R. Lima, H. T. Gomes and A. M. T. Silva, *Mater. Sci. Eng., C*, 2018, **93**, 206–217.

46 M. Gisbert-Garzarán, M. Manzano and M. Vallet-Regí, *Bioengineering*, 2017, **4**(1), 3.

47 M. L. Bruschi, *Strategies to Modify Drug Release from Pharmaceutical Systems*, 2015, pp. 63–86.

48 M. P. Paarakh, P. A. Jose, C. M. Setty and G. V. Peter, *Int. J. Pharm. Res. Technol.*, 2019, **8**, 12–20.

49 N. A. Peppas and B. Narasimhan, *J. Controlled Release*, 2014, **190**, 75–81.

50 M. H. Shoaib, S. Al Sabah Siddiqi, R. I. Yousuf, K. Zaheer, M. Hanif, S. Rehana and S. Jabeen, *AAPS PharmSciTech*, 2010, **11**, 708–718.

51 J. L. Diaz de Tuesta, B. F. Machado, P. Serp, A. M. Adrián, J. L. Faria and H. T. Gomes, *Catal. Today*, 2020, **356**, 205–215.

52 A. Quintanilla, J. L. Diaz de Tuesta, C. Figueruelo, M. Munoz and J. A. Casas, *Catalysts*, 2019, **9**, 516.

53 A. K. Nayak, D. Pal and K. Santra, *Int. J. Biol. Macromol.*, 2016, **82**, 1023–1027.

54 A. Khan, M. Iqbal Ch, J. Khan, G. Majid Khan, M. Hanif and A. Khan, *Lat. Am. J. Pharm.*, 2015, **34**, 277–282.

55 A. R. Fernandes, J. Dias-Ferreira, C. Cabral, M. L. Garcia and E. B. Souto, *Colloids Surf., B*, 2018, **166**, 24–28.

56 P. Costa and J. M. Sousa Lobo, *Eur. J. Pharm. Sci.*, 2001, **13**, 123–133.